Chinese Chemical Letters 33 (2022) 4197–4202

Contents lists available at ScienceDirect

Chinese Chemical Letters

journal homepage: www.elsevier.com/locate/cclet

Microenvironment-responsive chemotherapeutic nanogels for enhancing tumor therapy *via* DNA damage and glutathione consumption

Mengjie Ye[a], Yuan Gao[a], Mengyun Liang[a], Wei Qiu[a], Xianbin Ma[a], Jiming Xu[a], Junfeng Hu[a], Peng Xue[a], Yuejun Kang[a], Zhigang Xu[a,b,*]

[a] *Key Laboratory of Luminescence Analysis and Molecular Sensing (Southwest University), Ministry of Education, School of Materials and Energy and Chongqing Engineering Research Center for Micro-Nano Biomedical Materials and Devices, Southwest University, Chongqing 400715, China*
[b] *Key Laboratory of Laser Technology and Optoelectronic Functional Materials of Hainan Province, College of Chemistry and Chemical Engineering, Hainan Normal University, Haikou 571158, China*

ARTICLE INFO

Article history:
Received 15 September 2021
Revised 27 January 2022
Accepted 28 January 2022
Available online 4 February 2022

Keywords:
Nanogel
Prodrug
GSH-responsive
DNA damage
Chemotherapy

ABSTRACT

Although targeted therapy and immunotherapy are now shining in the treatment of some cancers, chemotherapy is still the cornerstone of drug treatment for many cancer patients. The emergence of chemotherapy prodrugs can improve the drug activity and reduce the side effects of chemotherapy. When used, the tumor microenvironment has characteristics different from normal tissues, and the existence of the microenvironment provided a more convenient way to design responsive nanodrugs. Herein, we designed a glutathione (GSH)-responsive prodrug nanogels for enhancing tumor chemotherapy. In the nanogels of HHNP, 10-hydroxycamptothecin (HCPT) played an essential role in killing cancer cells. HCPT was jointed with a cross-linker agent with disulfide bond and was further coated with polyethylene glycol, which not only prolonged the half-life of the drug, but also made HCPT accurate transport to the tumor fractions and achieved precise and controllable release. The proposal of HHNP effectively retained the biological activity of the drug, and introduced functions such as targeting, selective release and biodegradation, which greatly improved the medical efficiency of the drug and effectively reduced the toxic and side effects. This chemotherapeutic prodrug nanogel offers a new window for constructing efficient drug delivery platform.

Traditional cancer therapy strategies such as surgery [1], radiation therapy [2–4] and chemotherapy [5], have drawn more interest and achieve great clinical advances. Unluckily, chemotherapy drugs were mostly cytotoxic drugs, and can simultaneously damage to normal and tumor cells [6]. Therefore, the toxic side effects of drugs in practical applications have been criticized by cancer patients. In the past few decades, nanotechnology-based drug delivery systems (DDS) [7–11] have been developed that can respond to intracellular or extracellular stimuli such as pH [12–15], redox [16], enzymes [17,18], temperature [19–21], ultrasound [22,23], reactive oxygen species (ROS) [24–27]. As expected, such the stimuli-triggered DDS can selectively deliver drugs in tumor cells/tissues and drastically enhance the bioavailability and therapeutic outcome while markedly relieving the side-effect, representing a promising therapeutic strategy for cancer. However, some factors including complex building-up process and low efficiency *etc*. still postpone the clinic application of DDS, while simple but valid preparation strategy of DDS is urgently needed for regulation of cancer treatment.

Prodrug-based DDS is one importantly used approach for the delivering of drugs due to its high drug loading, stimuli-responsive drugs release and high antitumor efficiency. Many kinds of DDS based small molecular prodrug [28,29], polyprodrug [30–33] and liposome prodrug [34,35], *etc.* have also verified that prodrug approach can be an effective tool for enhancing the tumor accumulation and therapeutic efficacy. As a natural camptothecin analogue, 10-hydroxycamptothecin (HCPT) was a promising anti-cancer ingredient with extensive anti-tumor activity [36,37]. Its therapeutic mechanism was based on stabilizing the cleavable complex to inhibit DNA S-phase replication and RNA transcription, thereby targeting the ribozyme topoisomerase I (Topo I) and subsequently causing DNA damage/cleavage [38–40]. However, the clinical application of HCPT was limited by poor water solubility, side ef-

* Corresponding author.
E-mail address: zgxu@swu.edu.cn (Z. Xu).

https://doi.org/10.1016/j.cclet.2022.01.086
1001-8417/

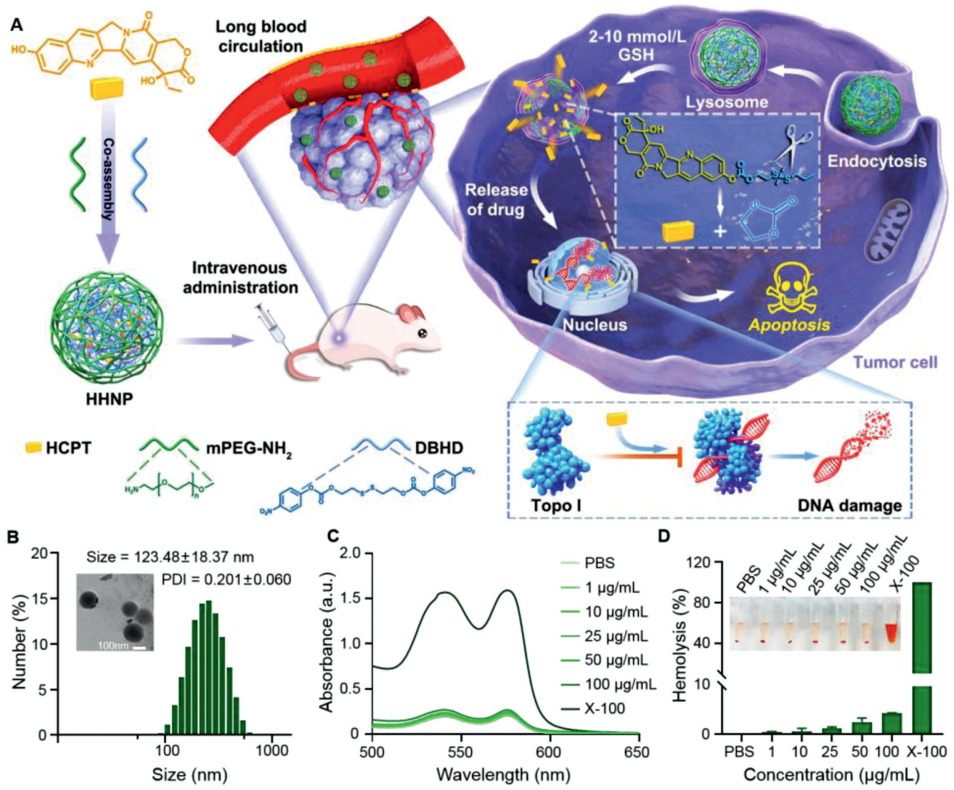

Fig. 1. (A) Synthesis of reductive-responsive chemotherapeutic nanogels and application in enhanced chemotherapy. (B) DLS size distribution histogram and TEM image of HHNP. (C) UV absorption spectra and (D) Hemolysis rate of different concentrations of HHNP, PBS, 0.1% Triton X-100 and blood cells after incubation. Data are presented as mean ± SD ($n = 3$).

fects and instability *in vitro* and *in vivo*. An in-depth understanding on mechanism of chemotherapeutics can inspire us for designing a new prodrug strategy for the development of chemotherapeutic nanomedicine [41,42].

Herein, a tumor GSH-responsive PEGylation nanomicelles based prodrug strategy (designated as HHNP) was constructed to achieve enhanced chemotherapy (Fig. 1A). The prodrug nanogel HHNP, were prepared by covalently combining the cross-linker agent with the topoisomerase-type chemotherapeutic drug HCPT, and then modified with PEG-NH_2 to improve its water solubility and biocompatibility. HCPT can be rapidly released by the reduction-triggered cleavage of the disulfide bond and enter into 4T1 cells to prevent DNA reconnection and induce DNA damage, thereby inducing cancer cell apoptosis. Therefore, such chemotherapeutic nanogel may offer an alternative method to promote the development of prodrug-based drug delivery system for cancer therapy in annoying microenvironments.

In the circulation of drugs in the blood, the key point for the effector drugs to accumulate in the tumor fraction is the size of the prepared nanogels. We could obtain the particle size distribution map of HHNP through the dynamic light scattering (DLS), and the size and polydispersity index (PDI) were 123.48 ± 18.37 nm and 0.201 ± 0.060, respectively (Fig. 1B), which could endow HHNP with the ability of passively target tumors. From the ultraviolet spectrum (Fig. S1 in Supporting information), a strong absorption peak of HCPT appeared at 385 nm, and a strong absorption of HHNP appeared at the nearby position, which proved the successful loading of HCPT. These spectral data in combination with the infrared spectrum (Fig. S2 in Supporting information), the carbonyl peaks can be found in HCPT and HHNP at 1730.86 cm^{-1} and 1761.81 cm^{-1} respectively, totally confirmed that successful preparation of HHNP. Moreover, the transmission electron microscope (TEM) image showed that HHNP showed a uniform and regular spherical micelles with a size of about 130 nm, which was consistent with the DLS results. Meanwhile, there were no significant change for particle size and PDI in 10 days (Fig. S3 in Supporting information), indicating that HHNP had an excellent stability.

According to the formula of uploading capacity and encapsulation efficiency, it could be concluded that the loading capacity of HHNP was about 12.0%, and the encapsulation efficiency of HCPT was about 86.7%, indicating that the HHNP had a higher loading capacity and encapsulation efficiency (Fig. S4 in Supporting information). Notably, the disulfide bonds in cross-linkers were sensitive to the reductive microenvironment, and the release kinetics of HCPT from HHNP were evaluated in a simulated medium with different DTT concentration (Fig. S5 in Supporting information). The release amount of HCPT was within about 30% under PBS (pH 7.4) without DTT or with 2 μmol/L DTT. However, the maximum release could reach to about 75% under a high 2 mmol/L DTT medium, which showed that HHNP could achieve precise and controllable release, reducing the toxic and side effects of chemotherapy drugs on therapeutic process. We subsequently investigated the ability of HHNP to destroy red blood cells through hemolysis experiments. As shown in Figs. 1C and D, the upward tendency of the hemolysis rate was unconspicuous with the increased concentration of HHNP. When the concentration was 100 μg/mL, the hemolysis rate was also lower than 5%, and indicated that HHNP had good blood compatibility and was conducive to the long circulation of drugs.

Next, we evaluated the uptake effect of HHNP through a series of cell experiments. Firstly, Nile red dye was added in the process of synthesis to label HHNP for quantifying the percentage of phagocytic drugs. As shown in the Figs. 2A and B, the phagocytosis reached to 93.96% after incubated with the HHNP for 4 h, indicating that HHNP could fast enter into cells with a time-dependent

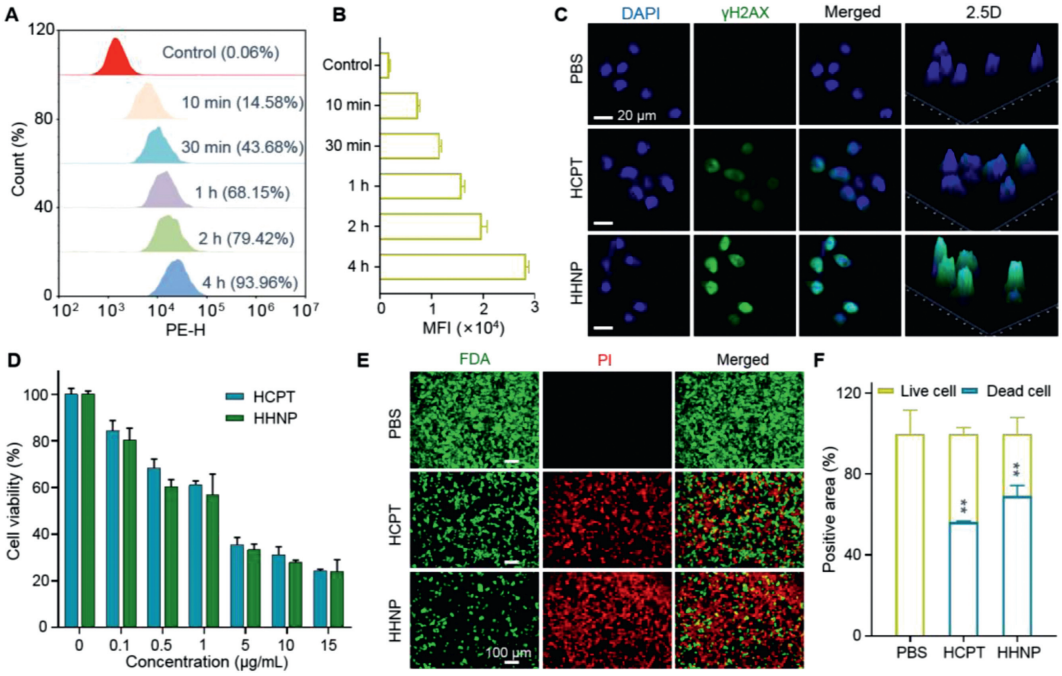

Fig. 2. Cellular uptake and cytotoxicity assays of HHNP in 4T1 cells. (A) Uptake of HHNP at different time points in the 4T1 cell with flow cytometry analysis and (B) quantification of cellular uptake in 4T1 cells. (C) Fluorescence imaging of DNA damage. (D) Cell viability of incubating with HCPT and HHNP for 72 h. (E) Distribution and (F) quantitative analysis of live and dead 4T1 cells after 24 h incubation with, free HCPT and HHNP. Data are presented as mean ± SD ($n = 3$). $^{*}P < 0.05$; $^{**}P < 0.01$.

manner. Considering the small size, it is necessary to investigate the intracellular distribution of HHNP. As shown in Fig. S6 (Supporting information), we could find that the drug was mainly rich in cytoplasm and nucleus. The subsequent co-localization technologies were further verified that HHNP could be passed into lysosomes and mitochondria after cell endocytosis, and the corresponding quantitative analysis also confirmed that the prolonged time would improve the uptake amount (Figs. S7 and S8 in Supporting information).

It plays a vital role in regulating the redox balance within the cell. Some studies had verified that GSH was closely related to the occurrence, development and metastasis of cancer. In addition, the high content of GSH in tumor cells will hinder a variety of cancer treatment strategies. It was a feasible strategy to consume GSH in cancer cells through disulfide cross-linkers and release drugs to improve the efficiency of cancer treatment [43–48]. Considering the high density of disulfide bonds in HHNP could consume the reductive GSH in tumor cells, we thus used a ThiolTracker Violet probe to assess the cellular level of reduced GSH. The 4T1 cells were incubated with PBS, HCPT, HHNP for 12 h (Fig. S9 in Supporting information), and the cells incubated without drugs showed strong green fluorescence, followed by HCPT, the weakest green fluorescence was in the HHNP group. A large amount of GSH in the cells was used to break the disulfide bond and consume GSH, release HCPT, and enhance the efficacy of chemotherapy.

As the core of drug delivery system, the therapeutic parameters occupy a key role in potential clinical application. Based on the good performance of intracellular distribution and GSH consumption, several assays including DNA damage, MTT, and live/dead were carried out to roundly evaluate the cytotoxicity effect and therapeutic mechanism. As the therapeutic engine of HHNP, HCPT can be targeted to the ribozyme topoisomerase I (Topo I), inhibiting DNA S-phase and RNA transcription, damaging DNA and killing cancer cells. As is shown in the Fig. 2C and Fig. S10 (Supporting information), the PBS group did not show any drug action or green fluorescence, whose nucleus was intact, proving that its DNA was integrated and undamaged. However, the HCPT and HHNP groups had no complete cell nucleus and stronger green fluorescence than that of PBS group. Compared with HCPT group, HHNP showed stronger green fluorescence, indicating that its higher DNA damage ability. This might be due to the PEGylation which endow drugs with improved hydrophilicity, enhancing the cell uptake and retention of drugs in cells, which played a synergistic effect for DNA damage.

Next, the MTT results shown in Fig. 2D demonstrated that HHNP had a strong lethality to 4T1 cells and obeyed a dose-dependent cytotoxicity. When the HHNP concentration was 15 μg/mL, the cell survival rate was reduced to 25%, indicating that the modification of PEG had negligible influence on the therapeutic effect of HCPT. Further, live/dead cell staining assay was used to intuitively observe the killing ability of HHNP on cells (Figs. 2E and F). Based on the quantitative results, the damage of HHNP to cells was about 10%, which was stronger than that of free drugs. All these results related cell toxicity and apoptosis demonstrated that HHNP could be as a high-efficiency anticancer agent for chemotherapy.

Even further, in order to cope with the complex environment in solid tumors and enhance the tumor inhibition rate, we constructed a 4T1 tumor sphere model to simulate subcutaneous tumors to detect the permeability of HHNP, laying the foundation for subsequent *in vivo* simulation treatments. As shown in Figs. 3A and B, from the two-dimensional plane of the tumor sphere stack fluorescence and 3D graphs, it could be seen that with the increase of the drug action time, the fluorescence intensity also had a significant increasing trend, and the penetration depth had also increased significantly, demonstrating the excellent penetration performance of HHNP.

The *in-vivo* biodistribution of the anti-cancer drug played a crucial role in the early treatment of mice body (Figs. 3C and D). The free DIR and HHNP were injected into the mice to observe the

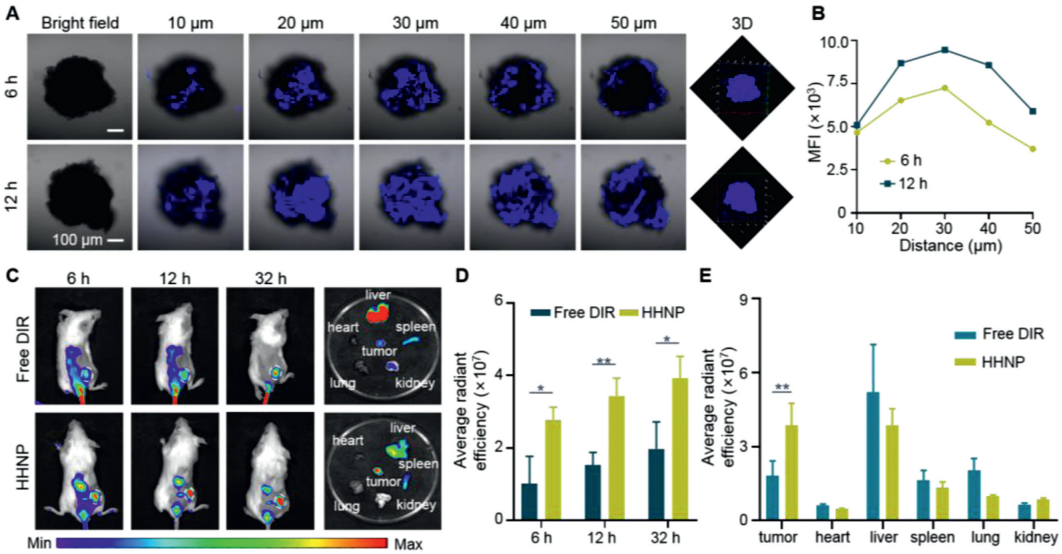

Fig. 3. Penetration imaging (A) and (B) fluorescence quantification of HHNP in the 4T1 tumor spheres for 6 and 12 h, respectively. (C) *In-vivo* fluorescence imaging and (D) average radiant fluorescence intensity of distribution in 4T1 mice model at 6, 12 and 32 h, respectively. (E) The fluorescence intensity of the tumor and five internal organs (heart, liver, spleen, lung, kidney) after injection of free DIR and HHNP. Data are presented as mean ± SD ($n = 3$). $^{*}P < 0.05$; $^{**}P < 0.01$.

drug distribution at different time periods. After the drug was injected intravenously, the drug with the stronger the fluorescence was accumulated at the tumor site by EPR (enhanced permeability and retention) effect [49–53]. Compared with free DIR group, HHNP group showed a stronger fluorescence in tumor site, which indicated that HHNP had exerted its nanoscale size effect and could be effectively aggregated at tumor tissue. More evidences could be observed that high and aggregated fluorescence in the liver, indicating that the drug was mainly excreted from the body through liver metabolism (Fig. 3E). The pharmacokinetics of HHNP was evaluated with SD mice. As is shown in the Fig. S11 (Supporting information), the longer blood circulation time was reflected, the half-life time of HHNP was about 1.40 h, indicating that the present HHNP strategy could improve the blood circulation time.

On the basis of better material capability and remarkable anticancer effect in extracorporeal cell experiments, in order to further explore the anticancer effect of HHNP in response to actual tumors, the 4T1 mice tumor model was established, and the tumor volume change and the weight of the mice were monitored in fixed time during the course of treatment. The animal experiments were performed the National Guide for the Care and Use of Laboratory Animals completely, and the agreement has passed through the Institutional Animal Care and the Southwest University Use Committee (IACUC). As we could see from the Fig. 4A, the 4T1 cells were injected subcutaneously into the mice, at –7 day, subsequently, the tumor volume grew to about 100 mm^3, and intravenous injection of drugs was started for group therapy. The entire course of treatment lasted 12 days. At the end of therapy, anatomy and tumor analysis were performed. As shown in the Figs. 4B and C, there were significant differences in the volume of mice in the four different treatment groups. The volume of mice injected with normal saline increased rapidly, while the volume of other drug-injected groups showed a slowdown. Among them, the volumes of mice injected with HHNP were growth retardation, exhibiting outstanding antitumor capability. There was no dramatic difference in body weight of mice during treatment period (Fig. 4D). The tumor quality was consistent with the tumor volume results, and the HHNP group showed a stronger tumor suppressing effect (Figs. 4E and F). After treatment, there was no remarkable difference in the quality of the five internal organs in different groups, demonstrating the better biological safety of HHNP (Fig. S12 in Supporting information).

The survival experiment of mice was based on *in vivo* treatment. After the injection, the tumor growth would continue to be observed, and the mice that had not undergone any drug treatment were sacrificed first, followed by free HCPT, finally the group of HHNP were sacrificed (Fig. 4G). The reason that HCPT group was sacrificed before the DOXIL group might be due to the poor continuous treatment effect of the HCPT group, and the removal rate of DOXIL was slower because it was coated with liposomes. It could also be seen from the tumor volume graphs treated in mice that the tumor growth trend of DOXIL slows down after re-administration. In the survival stage, the body weight of the mice in the treatment group and the non-treatment group did not significantly decrease (Fig. S13 in Supporting information). After normal treatment, the tumors were made into CD31, hematoxylin-eosin (H&E), Ki67, TdT-mediated dUTP nick-end labeling (TUNEL) stained sections (Figs. 4H and I). From the quantification, as is shown in the Figs. 4J and K and Fig. S14 (Supporting information), the HHNP group had the best therapeutic effect, with the majority of apoptotic cells and the least vascular proliferation. Increased DNA damages were also shown in 4T1 cells by treatment with HHNP with a level much higher than that treated with HCPT, DOXIL at the same concentration dose, clarifying that HHNP could significantly improve the side effects and hydrophobicity for further enhancing DNA damages and prevented DNA repair (Figs. S15 and S16 in Supporting information). There are no obvious pathological abnormalities in the sections of the five internal organs (Fig. S17 in Supporting information), and the blood routine indexes and body weights of Balb/C mice on the first and seventh days with Saline, DOXIL, HCPT, HHNP fluctuated within the normal range (Fig. S18 in Supporting information), indicating that HHNP had good biocompatibility.

In this study, we designed a GSH-responsive chemotherapeutic nanogel to enhance tumor chemotherapy. The first-line chemotherapy drug HCPT was encapsulated in the nanogels using disulfide bonds-based cross-linker. By means of prodrugs, HHNP passively target and accumulate to the tumor fraction, and the tumor microenvironment responded to the controllable release of the drug. The HHNP showed excellent therapeutic effect at the cellular and *in vivo* levels. More important, the nanodrug could markedly pro-

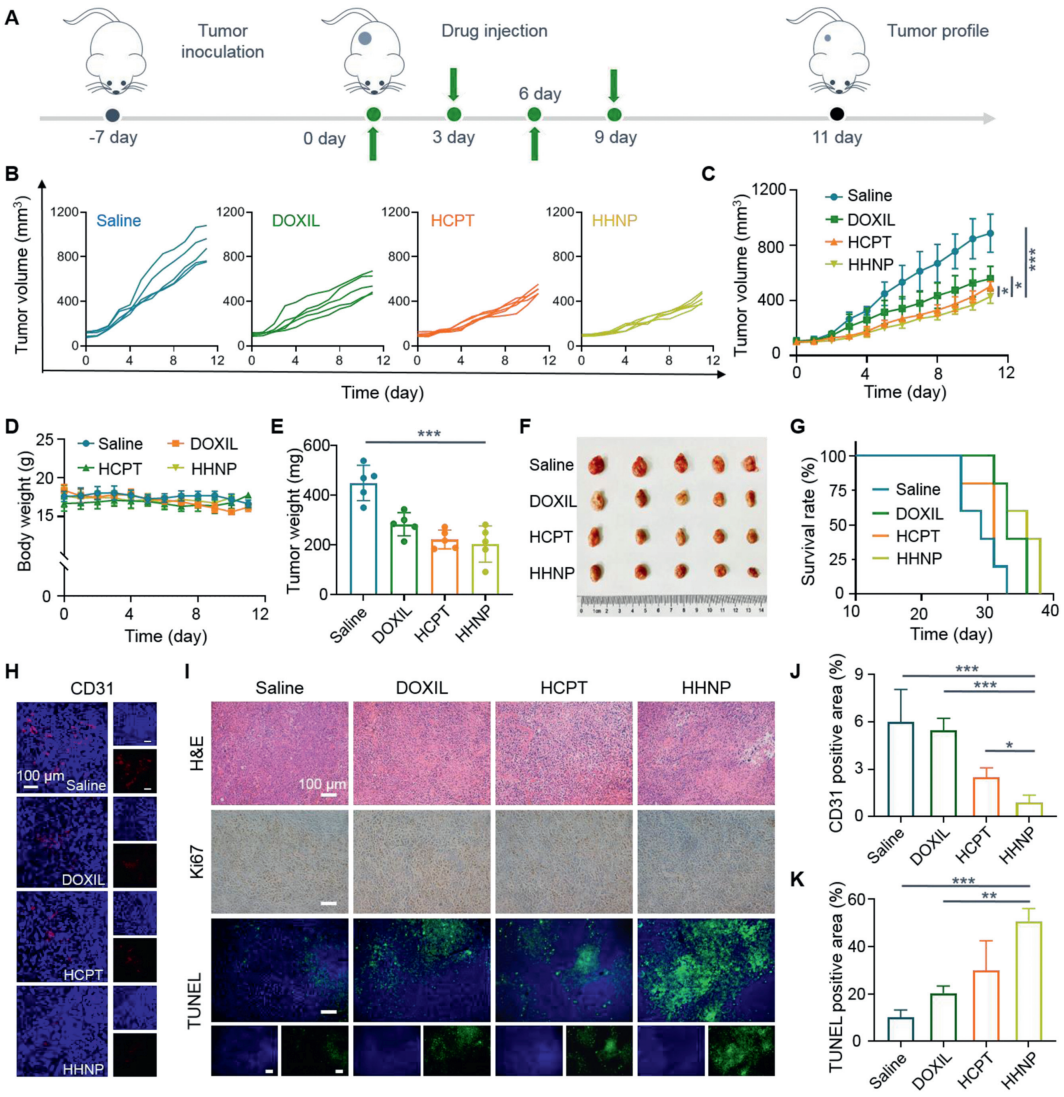

Fig. 4. *In vivo* treatment of HHNP on 4T1 tumor-bearing mice. (A) Course of treatment in 4T1 tumor-bearing mice. (B) Tumor volume changes during 11 days of treatment in various groups. (C) Average tumor volume changes. (D) Average body weight changes. (E) Tumor quality in various drug groups after treatment. (F) Digital images and (G) survival curve of the various drug groups ($n = 5$). (H) Quantification the fluorescence changes in CD31 slice images and (I) H&E, Ki67 and TUNEL slice images. (J) Quantification of CD31 and (K) TUNEL in tumor tissue sections from mice after treatments. Data are presented as mean ± SD ($n = 3$). $^{*}P < 0.05$; $^{**}P < 0.01$; $^{***}P < 0.001$.

long the survival time of tumor-bearing mice and showed an excellent *in-vivo* biological safety. The design can promote the development of chemotherapy prodrugs, offering a way for the development of chemotherapeutic drug delivery system.

Declaration of competing interest

The authors declare that they have no known competing financial interests or personal relationships that could have appeared to influence the work reported in this paper.

Acknowledgments

This work was financially supported by the Chongqing Graduate Program of Research and Innovation (No. CYS21110), the National Natural Science Foundation of China (Nos. 51703187, 32071375), Chongqing Talents of Exceptional Young Talents Project, China (Nos. CQYC202005029 and cstc2021ycjh-bgzxm0061). We thank Dr. Bi-Yue Ding (Southwest University) for providing valuable technical assistance in using IVIS Lumina imaging system.

Supplementary materials

Supplementary material associated with this article can be found, in the online version, at doi:10.1016/j.cclet.2022.01.086.

References

[1] S. Quader, K. Kataoka, Mol. Ther. 25 (2017) 1501–1513.
[2] K. Cheng, M. Sano, C.H. Jenkins, et al., ACS Nano 12 (2018) 4946–4958.
[3] S. Goel, D. Ni, W.B. Cai, et al., ACS Nano 11 (2017) 5233–5237.
[4] M.A. Knoll, R. Jagsi, K. Rosenzweig, JAMA Oncol. 5 (2019) 442.
[5] K. Li, C.C. Lin, Y. He, et al., ACS Nano 14 (2020) 14164–14180.
[6] S. Bai, L.L. Yang, Y.J. Wang, et al., Small 16 (2020) 2000214.
[7] W. Ma, Q. Chen, W. Xu, et al., Nano Res. 14 (2020) 846–857.
[8] G. Chen, Y. Yang, Q. Xu, et al., Nano Lett. 20 (2020) 8141–8150.
[9] M. He, L. Yu, Y. Yang, et al., Chin. Chem. Lett. 31 (2020) 3178–3182.
[10] L. Yu, Z. Wang, Z. Mo, et al., Acta Pharm. Sin. B 11 (2021) 2004–2015.
[11] Y.Y. Yang, X. Liu, W. Ma, et al., Biomaterials 265 (2021) 120456.
[12] F. Ding, X.H. Gao, X.G. Huang, et al., Biomaterials 245 (2020) 119976.
[13] W. Tao, J.Q. Wang, W.J. Parak, et al., ACS Nano 13 (2019) 4876–4882.
[14] Q.W. Tian, Y.P. Li, S.S. Jiang, et al., Small 15 (2019) 1902926.
[15] W. Wu, L. Luo, Y. Wang, et al., Theranostics 8 (2018) 3038–3058.
[16] S.L. Li, P.E. Saw, C.H. Lin, et al., Biomaterials 234 (2020) 119760.
[17] B. Fejerskov, M.T.J. Olesen, A.N. Zelikin, Adv. Drug Deliv. Rev. 118 (2017) 24–34.
[18] R. Mooney, A.A. Majid, J. Batalla, et al., Adv. Drug Deliv. Rev. 118 (2017) 35–51.
[19] W.B. Hu, P.N. Prasad, W. Huang, Acc. Chem. Res. 54 (2021) 697–706.

[20] C.N. Xu, Y.B. Wang, E.L. Wang, et al., Adv. Funct. Mater. 31 (2020) 2009314.
[21] H. Zhao, J.B. Xua, J.S. Wan, et al., Nano Today 36 (2021) 101058.
[22] G. Canavese, A. Ancona, L. Racca, et al., Chem. Eng. J. 340 (2018) 155–172.
[23] Y. Yoon, W. Tang, X.Y. Chen, Small Methods 1 (2017) 1700173.
[24] Y.E. Gao, S.X. Hou, J.Q. Cheng, et al., ACS Sustain. Chem. Eng. 9 (2021) 3213–3222.
[25] S.X. Hou, Y.E. Gao, X.B. Ma, et al., Chem. Eng. J. 416 (2021) 129037.
[26] D. Jia, X.B. Ma, Y. Lu, et al., Chin. Chem. Lett. 32 (2021) 162–167.
[27] H. Guo, F.P. Li, W.G. Xu, et al., Adv. Sci. 5 (2018) 1800004.
[28] K. Zhang, Y. Zhang, X. Meng, et al., Biomaterials 185 (2018) 301–309.
[29] L. Feng, M. Gao, D. Tao, et al., Adv. Funct. Mater. 26 (2016) 2207–2217.
[30] B. Cao, F. Xiao, D. Xing, et al., Small 14 (2018) 1802008.
[31] P. Zheng, Y. Liu, J. Chen, et al., Chin. Chem. Lett. 31 (2020) 1178–1182.
[32] H. Huang, L. Mao, Z.H. Li, et al., J. Bioresour. Bioprod. 4 (2019) 231–241.
[33] X. Hu, S. Zhai, G. Liu, et al., Adv. Mater. 30 (2018) 1706307.
[34] M. Jiang, J. Mu, O. Jacobson, et al., ACS Nano 14 (2020) 16875–16886.
[35] W. Shen, W. Liu, H. Yang, et al., Biomaterials 178 (2018) 706–719.
[36] J.N. Li, W.G. Xu, D. Li, et al., ACS Nano 12 (2018) 6685–6699.
[37] L.J. Zhang, X. Zhang, G.H. Lu, et al., Small 15 (2019) 1805544.
[38] W. Jiang, Q. Li, L. Xiao, et al., ACS Nano 12 (2018) 5684–5698.
[39] K. Duskova, P. Lejault, É. Benchimol, et al., J. Am. Chem. Soc. 142 (2020) 424–435.
[40] U.S. Srinivas, B. Tan, B.A. Vellayappan, et al., Redox Biology 25 (2019) 101084.
[41] G. Barouti, C.G. Jaffredo, S.M. Guillaume, Prog. Polym. Sci. 73 (2017) 1–31.
[42] W.W. Mu, Q.H. Chu, Y.J. Liu, et al., Nano-micro Lett. 12 (2020) 142.
[43] J.S. Lan, L. Liu, R.F. Zeng, et al., Chem. Eng. J. 407 (2021) 127212.
[44] X.Y. Zhong, X.W. Wang, L. Cheng, et al., Adv. Funct. Mater. 30 (2019) 1907954.
[45] Y. Lu, D. Jia, X.B. Ma, et al., ACS Appl. Mater. Interfaces 13 (2021) 8940–8951.
[46] X.B. Ma, S.C. Yang, T. Zhang, et al., Acta Pharm. Sin. B 12 (2022) 451–466.
[47] Y.J. Wang, M.H. Zu, X.B. Ma, et al., ACS Appl. Mater. Interfaces 12 (2020) 50896–50908.
[48] H.G. Xiong, X.B. Ma, X.L. Wang, et al., Adv. Funct. Mater. 31 (2021) 2100007.
[49] R. Liu, M.N. Yu, X.T. Yang, et al., Adv. Funct. Mater. 29 (2019) 1808462.
[50] S. Wang, P. Huang, X.Y. Chen, Adv. Mater. 28 (2016) 7340–7364.
[51] P. Zheng, Y. Liu, J.X. Ding, et al., Chin. Chem. Lett. 31 (2020) 1178–1182.
[52] X.X. Shi, Y. Zhang, Y. Tian, et al., Small Methods 5 (2021) 2000416.
[53] Q.W. Zhu, M. Saeed, H.J. Yu, et al., Chin. Chem. Lett. 31 (2020) 1051–1059.